MATERIALS SCIENCE

Low-temperature 3D printing of transparent silica glass microstructures

Mingzhe Li[1]†, Liang Yue[1]†, Arunkumar Chitteth Rajan[2], Luxia Yu[1], Harikrishna Sahu[2], S. Macrae Montgomery[1], Rampi Ramprasad[2], H. Jerry Qi[1]*

Transparent silica glass is one of the most essential materials used in society and industry, owing to its exceptional optical, thermal, and chemical properties. However, glass is extremely difficult to shape, especially into complex and miniaturized structures. Recent advances in three-dimensional (3D) printing have allowed for the creation of glass structures, but these methods involve time-consuming and high-temperature processes. Here, we report a photochemistry-based strategy for making glass structures of micrometer size under mild conditions. Our technique uses a photocurable polydimethylsiloxane resin that is 3D printed into complex structures and converted to silica glass via deep ultraviolet (DUV) irradiation in an ozone environment. The unique DUV-ozone conversion process for silica microstructures is low temperature (~220°C) and fast (<5 hours). The printed silica glass is highly transparent with smooth surface, comparable to commercial fused silica glass. This work enables the creation of arbitrary structures in silica glass through photochemistry and opens opportunities in unexplored territories for glass processing techniques.

INTRODUCTION

Glass is among the most indispensable materials in numerous advanced engineering applications due to its exceptional optical transparency, thermal and chemical stability, and chemical tunability (*1*–*4*). However, processing glass into desired shapes, particularly complex and miniaturized three-dimensional (3D) ones, is challenging compared to polymers and metals (*5*, *6*). Several advanced methods have been developed for glass manufacturing, such as injection molding (*7*), soft replication (*8*), laser-assisted etching (*9*), chemical vapor deposition (CVD) (*10*), and origami-based folding (*11*). Although these methods are well explored and demonstrate considerable potential, they have notable limitations. Injection molding and soft replication methods are unable to produce arbitrary 3D shapes with interpenetrating gaps such as lattices. Etching method involves the use of hazardous chemicals such as hydrofluoric acid and requires substantial postprocessing. CVD method often entails the use of complex facilities and compromises fabrication precision. Origami glass–making technique is restricted to specific 3D geometries that can be folded from planar sheets. Therefore, there is still a substantial need to develop new methods with mild conditions for fabricating glass.

Recent advances in additive manufacturing (AM), also known as 3D printing, have facilitated the development of simple yet effective glass fabrication techniques. These methods use a transparent photocurable nanocomposite resin, consisting of silica nanoparticles through direct mixing (*6*, *12*–*15*) or sol-gel in situ–generated silica (*16*) and a liquid monomeric matrix, as the "ink" for 3D printing. With the aid of stereolithography (*6*), digital light processing (*12*, *16*), two-photo polymerization (2PP) (*13*, *14*), or computed axial lithography (*15*) techniques, the photoresin is polymerized and shaped into structures as designed. The printed "green part" is then subjected to a pyrolysis process to remove the polymeric matrix binder through thermal decomposition, followed by high-temperature sintering to fuse the remaining silica nanoparticles together (*6*, *15*). Intricate glass architectures of superior quality can be produced using these methods (*13*, *14*). However, all these techniques use the formulation of nanoparticle-based photoresin and focus on pushing the boundaries of printing quality via different shaping techniques. The exploration of low-thermal or even nonthermal processes for converting the polymeric green part into silica glass has long been a challenge, inhibiting the establishment of a sustainable and resource-efficient glass economy. Specially, the pyrolysis and sintering processes used in these methods are time-consuming, taking more than 12 hours or even days (*15*, *17*), and require significant amounts of energy with temperatures exceeding 1100°C (*6*, *13*). Therefore, there is a considerable demand for low-thermal or even nonthermal 3D printing techniques that can fabricate high-performance silica structures cost-effectively. For example, a unique sinterless route can bring the processing temperature down to 650°C, enabling free-form printing of silica structures directly into microsystems (*18*).

The emerging technology using photochemistry-based conversion process has sparked growing interests in the field of electronic engineering (*19*) and hold tremendous potential for bridging the gap in low-temperature 3D printing of silica glasses. It is found that deep ultraviolet (DUV) irradiation can effectively induce organic to inorganic transformation, creating a metal-oxide network (*20*). Silica film can be generated from cross-linked polydimethylsiloxane (PDMS) using a DUV lamp in air (*21*–*23*). However, the application of DUV irradiation to convert PDMS into SiO_2 has been limited as a surface modification technique (*24*) and has not yet been applied to fabricate arbitrary SiO_2 structures through AM. In this work, we report a photochemistry-based strategy for 3D printing of silica glass structures of micrometer size (microstructures). We use a photosensitive PDMS resin as the ink, without the inclusion of silica nanoparticles. The PDMS resin is then shaped into desired microstructures via 2PP printing

[1]The George W. Woodruff School of Mechanical Engineering, Georgia Institute of Technology, Atlanta, GA 30332, USA. [2]School of Materials Science and Engineering, Georgia Institute of Technology, Atlanta, GA 30332, USA.
*Corresponding author. Email: qih@me.gatech.edu
†These authors contributed equally to this work.

technique. The 2PP-printed PDMS microstructure is converted into silica glass through a DUV lamp in an oxygen environment. The maximum processing temperature is around 220°C, and the process takes less than 5 hours. We confirm the conversion into silica glass using a series of chemical characterization techniques. Furthermore, we showcase various complex 3D glass microstructures with high precision and quality fabricated using this approach. The printed silica glass has extensive applications in optics, microfluidics, medical devices, and various other fields.

RESULTS

3D printing and processing of transparent silica glass

Our approach combines 2PP technique for high-precision printing of PDMS 3D microstructures and DUV-ozone processing method for full conversion of PDMS into silica glass. Figure 1A provides a schematic illustration of the 2PP printing process. A droplet of PDMS photoresin is placed on an indium tin oxide (ITO)–coated glass substrate that has been cleaned with oxygen plasma and silanized to ensure adequate adhesion to the printed structures. An infrared femtosecond laser beam with a wavelength of 780 nm is focused through a 25× microscope objective that is dipped into the liquid resin, creating a highly confined spatial region around the focal point where the light intensity exceeds the two-photon absorption threshold (*25*). Simultaneously, the photoinitiator in the resin absorbs the two photons and initiates the polymerization reaction, converting the liquid PDMS resin into a solid PDMS network. The designed PDMS microstructure is then printed layer-by-layer by scanning the focused beam inside the resin using an *x*-*y* galvanometer and a *z*-axis linear stage. Last, the PDMS structure is rinsed with SU-8 developer and isopropyl alcohol to remove unpolymerized excess resin and dried slowly at ambient conditions.

The 2PP-printed PDMS microstructure is then converted into a piece of transparent silica glass through a DUV-ozone treatment process as depicted in Fig. 1B. The DUV source used in this process is a xenon lamp emitting high-intensity (15 J per pulse at 100 Hz) and broad-spectrum [190 to 800 nm with the effective range of 190 to 254 nm; (*23*)] pulsed light. The PDMS microstructure is irradiated with the DUV source at a distance of 5 mm in a customized glass chamber. To produce fast and complete conversion, the glass chamber is continually purged with purified oxygen. Upon DUV irradiation, the oxygen molecule dissociates, leading to the generation of ozone. Ozone is a key intermediate, and it is further photodissociated into O_2 and singlet atomic oxygen $O(^1D)$ in excited state (*21*). The highly oxidative singlet atomic oxygen $O(^1D)$, which is the primary reactant, attacks the Si—C bond in PDMS molecules, leading to the substitution of the methyl groups with hydroxyl groups. Subsequently, the high-intensity DUV light–induced moderate temperature rise (~220°C as

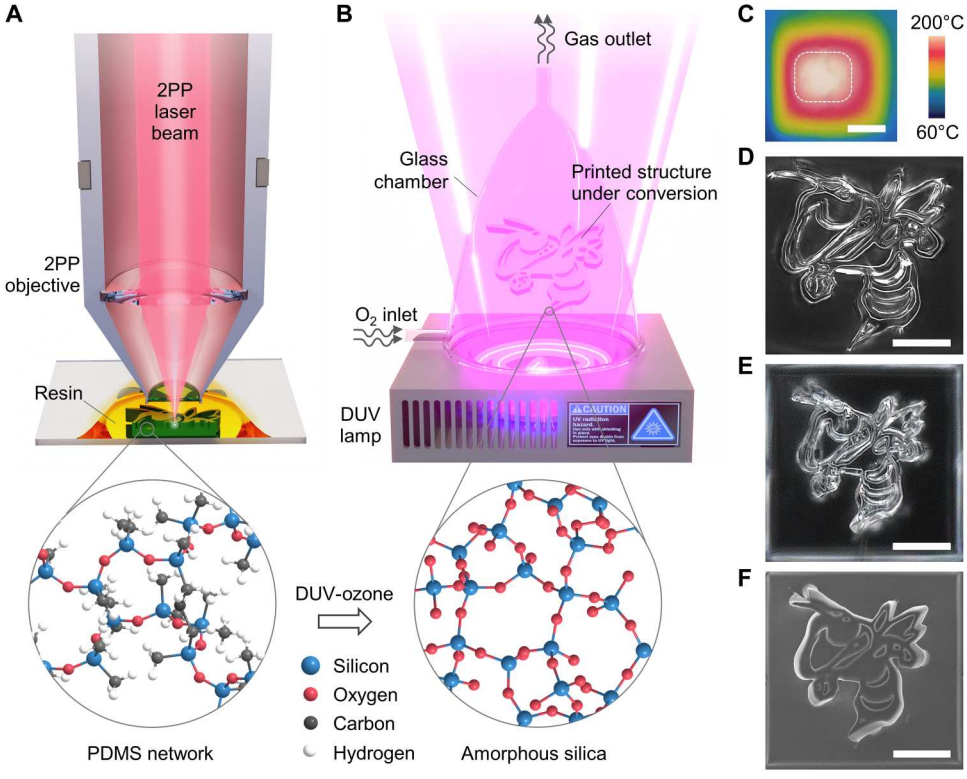

Fig. 1. Fabrication of transparent silica glass. (**A**) Schematic illustration of the 3D printing process to create microstructures with a PDMS network using a Nanoscribe 2PP printer. (**B**) Schematic illustration of the conversion process from PDMS to amorphous silica glass under DUV-ozone conditions. Oxygen is flowed continually into the glass chamber for the formation of ozone and singlet atomic oxygen $O(^1D)$ in excited state during DUV irradiation. (**C**) Infrared image of a thin film under DUV-ozone conversion. The white dash line indicates the position of the 3 cm–by–2.5 cm film. The temperature variation across the entire film is less than 20°C. Scale bar, 2 cm. (**D**) Optical microscope image of the printed PDMS Georgia Tech Buzz mascot before conversion. (**E** and **F**) Optical microscope image and scanning electron microscopy (SEM) image of the silica glass Buzz mascot after conversion. Scale bars, 50 μm.

shown in Fig. 1C and fig. S1) facilitates the dehydroxylation of neighboring silanol groups and prompts the formation of Si—O—Si bonds. Both DUV and ozone are indispensable in this conversion process (fig. S2). As the DUV irradiation proceeds, the PDMS microstructure is almost completely transformed into silica glass. Using this approach, we successfully fabricated silica glass microstructures free from voids or structural cracks. Figure 1D shows the optical image of 2PP-printed Georgia Tech "Buzz" mascot with dimensions of 140 μm by 160 μm by 20 μm before DUV-ozone conversion. Figure 1 (E and F) displays the optical and scanning electron microscopy (SEM) images of the converted silica Buzz. It shows increased light reflection and isotropic linear shrinkage compared to that before conversion. The finest resolution of the printed silica Buzz after DUV-ozone conversion at the sting is below 800 nm (fig. S3), and further enhancement of resolution below 200 nm is possible by using a 63× high magnification objective and high-precision piezo-stage control (*13*).

Chemical and physical characterizations of the printed silica glass

To better understand the conversion process, we perform first-principles density functional theory (DFT) calculations. Our results in Fig. 2A show that thermodynamics favors the progressive substitution of the methyl groups in the PDMS network by hydroxyl groups, leading to the formation of poly(dihydroxylsiloxane). Subsequent dehydration process results in the final SiO_2 3D structure. Three different reaction schemes have been considered and generate the same silica product (fig. S4). The detailed reaction pathway from DFT calculations reveals that the singlet atomic oxygen $O(^1D)$ generated from ozone photodissociation is critical for the initiation of the substitution reaction. To experimentally verify the conversion pathway, we use a suite of techniques to characterize the converted material. A thin free-standing PDMS film is fabricated and exposed to DUV irradiation for a predetermined duration of time. The thickness of the film is about 50 μm (fig. S5). Fourier-transform infrared spectroscopy (FTIR) is used to examine the formation of silanol groups and the dehydroxylation process. Figure 2B displays the FTIR transmission spectra ranging from 2800 to 3800 cm^{-1}. The cross-linked PDMS exhibits two adjacent peaks centered at 2961 and 2905 cm^{-1}, corresponding to the symmetric and asymmetric stretching of the C—H bonds (*21*, *26*). With increasing irradiation time to 3 hours, these two peaks are diminished to almost zero, indicating the cleavage of Si—C bonds and removal of the methyl groups. The decrease and shift of the strong peak at 1257 cm^{-1} (fig. S6) originating from the C—H bending vibration (*27*) further corroborate the elimination of methyl groups. Moreover, a broad absorption band centered at 3350 cm^{-1} appears upon initial DUV exposure, revealing the formation of silanol groups (*21*). After reaching its maximum intensity at 1 hour, the O—H band gradually decreases to zero at 3 hours, due to the dehydration of neighboring silanol groups. The emerging and then disappearing band centered at 910 cm^{-1} corresponding to Si—OH stretching (*28*) also confirms this evolution path of silanol groups. Last, the converted material shows two primary bands: one centered at 1010 cm^{-1} with a shoulder at 1100 cm^{-1} associated with the asymmetric stretching of Si—O—Si bond and the other at 780 cm^{-1} corresponding to the bending vibration of the Si—O bond (*21*). These observations

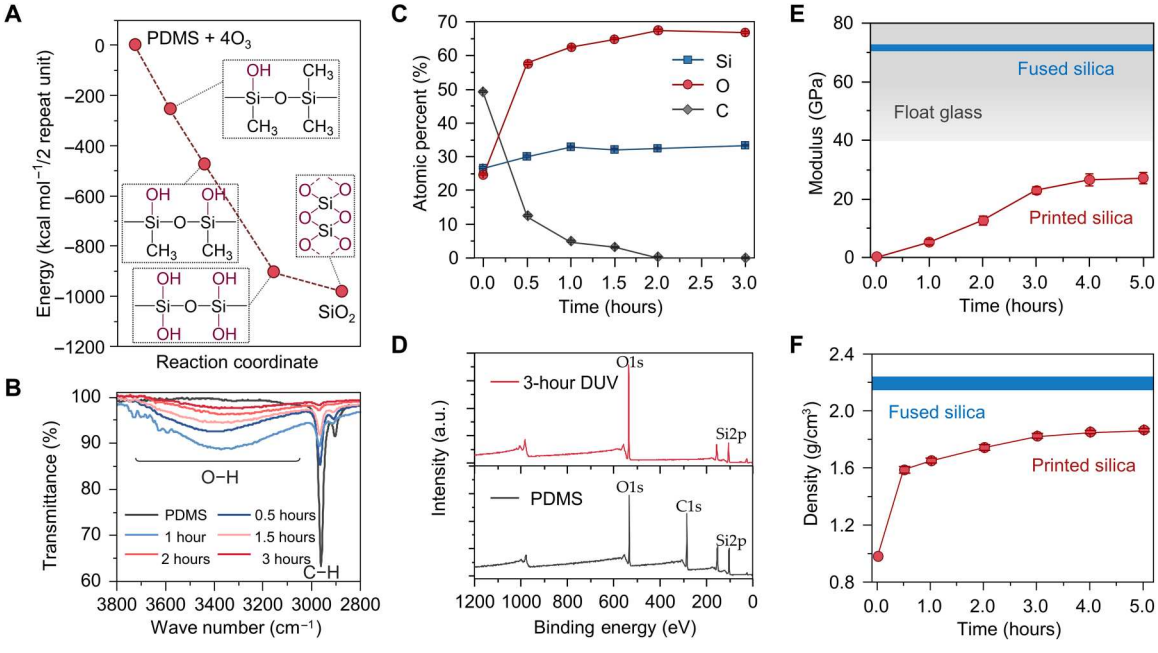

Fig. 2. Chemical and physical characterizations of the printed silica glass. (**A**) The reaction energy profile of PDMS conversion to silica glass computed using first principles thermodynamics density functional theory (DFT) calculations. (**B**) The FTIR spectra of the converted material after different DUV irradiation. (**C**) The atomic percent change of silicon, oxygen, and carbon in the converted material measured from x-ray photoelectron spectroscopy (XPS). (**D**) The comparison of the XPS spectra of neat PDMS and silica glass after 3-hour DUV conversion. The carbon peak is completely removed in the silica glass. a.u., arbitrary units. (**E**) The modulus of the converted material after different DUV irradiation measured from the peak force quantitative nanomechanical mapping (PF-QNM) technique in atomic force microscopy (AFM). (**F**) The measured density of the converted material after different DUV irradiation.

demonstrate that, after 3-hour DUV-ozone treatment, PDMS has been converted to silicon oxides, SiO_x.

The chemical composition of the converted material is quantitatively measured using x-ray photoelectron spectroscopy (XPS). The atomic percent change with varying irradiation time on the film front surface (Fig. 2C) and typical XPS spectra of both the PDMS film and converted material (Fig. 2D) are displayed. The characteristic peaks of silicon, oxygen, and carbon elements are observed in the PDMS film. Upon exposure to DUV, the intensity of the C1s peak decreases markedly while that of the O1s peak increases. After 2-hour DUV irradiation, the carbon element is reduced from 49 atomic % (at %) to almost zero, indicating the complete removal of carbon content on the front surface of the film. Simultaneously, the oxygen element percent gradually increases above 65 at %. After 3-hour treatment, the silicon and oxygen contents are 66.7 and 33.3 at %, respectively, achieving a Si:O ratio of 1:2, which confirms the formation of SiO_2 with a 100% conversion rate on the front surface. The shifts of the silicon peak also support the formation of SiO_2 (fig. S7). The binding energy of Si2p in PDMS is centered at 102.1 ev, which corresponds to the coordination of one silicon atom to two oxygen atoms (*29*). After 3-hour DUV irradiation, the Si2p peak shifts to 104.0 ev, indicating that silicon is coordinated to four oxygen atoms (*30*) as that in SiO_2. It is also noted that the oxygen environment and film thickness are critical parameters to achieve the full conversion (fig. S8), while the effect of different PDMS materials is secondary (fig. S9). X-ray diffraction (XRD) patterns (fig. S10) further confirm that the obtained silica is crystal-free and amorphous. Because the XPS detection depth is only a few nanometers, we further conduct XPS measurements on both the back surface and the cross section (fig. S11). The elemental analysis results indicate a similar trend of carbon percentage decrease, albeit at a slightly slower pace, on the back surface and cross section of the SiO_2 film (converted from the 50-μm-thick PDMS film). This is attributed to the diffusion-controlled conversion process, which involves the penetration of active singlet atomic oxygen into the film and the escape of carbon-containing gaseous phase out of the film. After 3-hour treatment, the carbon percentage drops to below 1.3 and 3.2 at % on the back surface and the cross section, respectively, indicating a relatively high conversion rate (>97%) across the entire film. It is observed that DUV penetration depth into the film is not a limiting factor here as the conversion at the film back surface starts as DUV irradiates. The conversion rate is further corroborated by thermal gravimetric analysis (TGA) (fig. S12). The obtained silica glass shows two main regions of mass loss: 300° to 500°C [~1 weight % (wt %)] due to the dehydroxylation of neighboring silanol groups and 500° to 900°C (~3 wt %) due to the degradation of the carbon-containing organic component (*31*). The overall mass loss of 4 wt % is consistent with XPS analysis. It is noted that, due to this incomplete conversion, the silica glass may further undergo subtle shrinkage above 300°C. Therefore, the converted silica may not be suitable for applications that require high thermal stability. Increasing DUV light intensity or optimizing DUV light spectrum can further promote the conversion rate to 100% to solve this problem.

The mechanical properties of the converted silica are characterized using an indentation-based peak force quantitative nanomechanical mapping (PF-QNM) technique in atomic force microscopy (AFM). The system is tuned and characterized before testing (see Materials and Methods and fig. S13). Figure 2E displays the modulus change of the printed silica as a function of increasing DUV irradiation time. After 3-hour treatment, the modulus is markedly enhanced to 22.9 GPa and eventually stabilized at around 27.1 GPa after 5 hours (fig. S14). While this value is lower than that of float glass (SiO_2-Na_2O-CaO-MgO, >40 GPa) and fused silica (SiO_2, 72 GPa), achieving such a level of modulus without high-temperature sintering induced densification is promising. The stiffness of our printed silica is similar to that of silica oxide films (18 to 43 GPa) fabricated by CVD and atomic layer deposition methods at relatively low temperature conditions (*32*–*34*). Two factors may contribute to the relatively low stiffness. First, the Si—O—Si chains are randomly packed upon conversion and not reconfigured to a dense state, creating vacancies at the molecular level that have negative impact on the mechanical properties. Besides, the residual carbon content in the printed silica could also function as a secondary factor. Both factors can also lead to the relatively low density of printed silica, which is measured (see Materials and Methods, fig. S15, and table S1) and shown in Fig. 2F. The density of PDMS is 0.97 g/cm^3. After 1-hour conversion, the mass is reduced by about 15% and the volume by 50%, resulting in a density of 1.65 g/cm^3. Further DUV-ozone treatment increases the density to about 1.85 g/cm^3, which is lower than that of fused silica (2.2 g/cm^3). These findings confirm the explanation given above. The obtained silica meets the criteria for various applications such as optical, chemical, and medical devices, but it may not be suitable to be used as load-carrying structural components due to the relatively low density and modulus. Additional heat treatment is required to achieve fully dense silica. Results show that subjecting the printed microstructure to a 1000°C treatment leads to nearly pure fused silica, with a density of ~2.16 g/cm^3 (fig. S16).

3D printing of silica glass microstructures

To demonstrate the capability of our approach, a number of microarchitectured silica structures with complexity and precision are fabricated. Figure 3 depicts representative SEM images of the printed microstructures before and after conversion. More printed microstructures are displayed in fig. S17. Specially, monolithic micropillars with diameter of 6 μm (Fig. 3A), woodpile microstructures with ellipsoid cross sections of around 8 μm (Fig. 3C), and octet microlattice with truss diameter of 5 μm (Fig. 3, E and G) are printed using PDMS resin. A solid PDMS base is printed in between the PDMS microstructures and the glass substrate to increase their adhesion and minimize their strain mismatch during DUV-ozone conversion. The quality and resolution of these microstructures match the state-of-the-art 2PP printings (*35*, *36*). To ensure full conversion of PDMS to silica, the feature sizes of these microstructures are much smaller than the PDMS film used in above chemical characterization. Exposure in DUV-ozone environment for 3 hours yields undistorted silica glass microstructures (Fig. 3, B, D, F, and H), showing a linear shrinkage of approximately 24% (see fig. S15 for detailed shrinking process during conversion), which is comparable to that of high-temperature sintering-involved 3D printed silica (*11*, *13*–*15*). The shrinkage is nearly isotropic, even in the vertical direction (fig. S18). Only minor nonuniform shrinkage at the interface between the printed structure and the base (Fig. 3D) is observed. This is due to the strain mismatch between the shrinking structure and the base, which can be mitigated by incorporating predesigned support structures such as hollow pedestals or coiled springs (*37*, *38*). The printed silica glass exhibits no

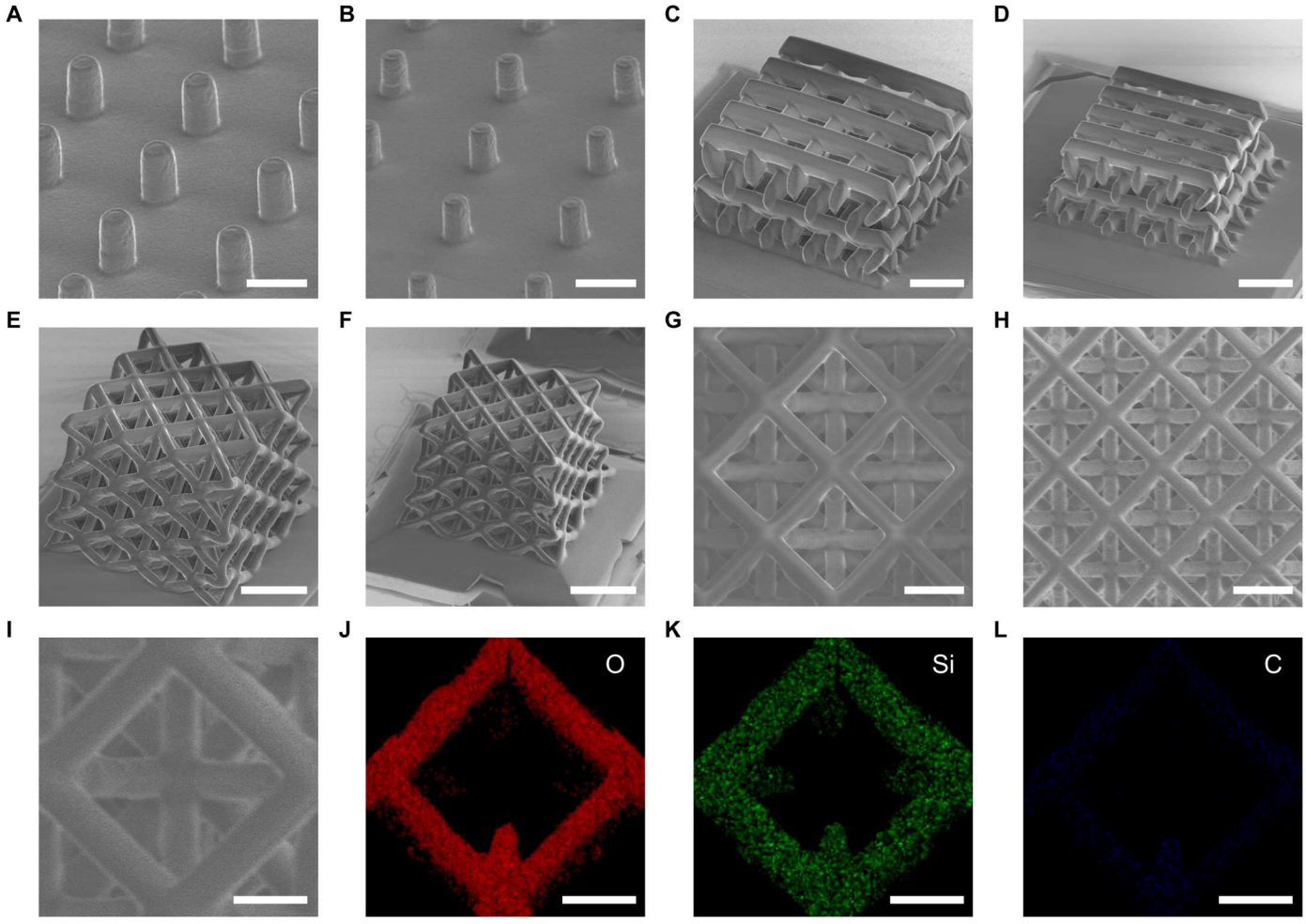

Fig. 3. 3D printed microstructures using the proposed technique. (**A** and **B**) Micropillar array before and after conversion. Scale bars, 20 μm. (**C** and **D**) Woodpile microstructure before and after conversion. Scale bars, 30 μm. (**E** and **F**) Octet microlattice before and after conversion. Scale bars, 50 μm. (**G** and **H**) Zoomed-in top view of the printed octet microlattice before and after conversion. Scale bars, 20 μm. (**I** to **L**) EDS mapping of the octet microlattice exhibiting uniform distribution of oxygen, silicon, and almost negligible carbon. Scale bars, 10 μm.

crack, pore, or flaw formation throughout the entire part. Energy-dispersive x-ray spectroscopy (EDS) mapping of the printed silica glass structure (Fig. 3, J and K) shows homogenous distribution of oxygen and silicon with no visible aggregation. After excluding the negligible amount of carbon (Fig. 3L) from analysis, the atomic percent of oxygen and silicon are 65.2 and 34.8%, respectively (fig. S19), corresponding to a Si:O ratio of 1:1.9. Considering that EDS has a low detection in measuring light elements (except carbon due to background counts and surface contamination), the oxygen may be underestimated relative to silicon. Therefore, this measured Si:O ratio agrees well with the results of XPS and TGA, further demonstrating the nearly full conversion to silica glass.

Applications of the 3D printed silica glass

As demonstrated above, our approach can fabricate high-precision silica glass microstructures with complex shapes. The printed silica glass can find broad applications in photonics, functional surfaces, and lab-on-a-chip devices. Here, we highlight the potential applications of the printed silica glass in micro-optics and microfluidics.

Miniaturized and highly integrated optical components are in great demand for imaging and beam shaping purposes in many medical, microelectronics, and research applications (*39*, *40*). For example, achieving noninvasive imaging at cellular resolution requires the miniaturization of the size of lenses in medical endoscopes to ~100-μm level (*41*). Silica glass material is widely used as optical lenses due to its high light transmission over a wide range of wavelengths. However, fabrication of silica glass lenses by conventional methods may require time-consuming grinding and polishing steps (*17*). Using our approach, silica glass microlenses can be successfully fabricated at optical surface quality under mild conditions.

A proof-of-concept silica glass lens with the size of 150 μm by 150 μm after DUV conversion in the convex-plano configuration is displayed in Fig. 4 (A and B). The microlens exhibit an exceptionally low arithmetic mean line roughness (R_a) of 1.5 nm (Fig. 4C), slightly lower than other 2PP-printed silica glasses with roughness <5 nm (*14*, *15*, *18*). We attribute this low roughness to the absence of silica nanoparticles in the photoresin. The unique optical transparency of the printed silica glass is evaluated using ultraviolet-visible

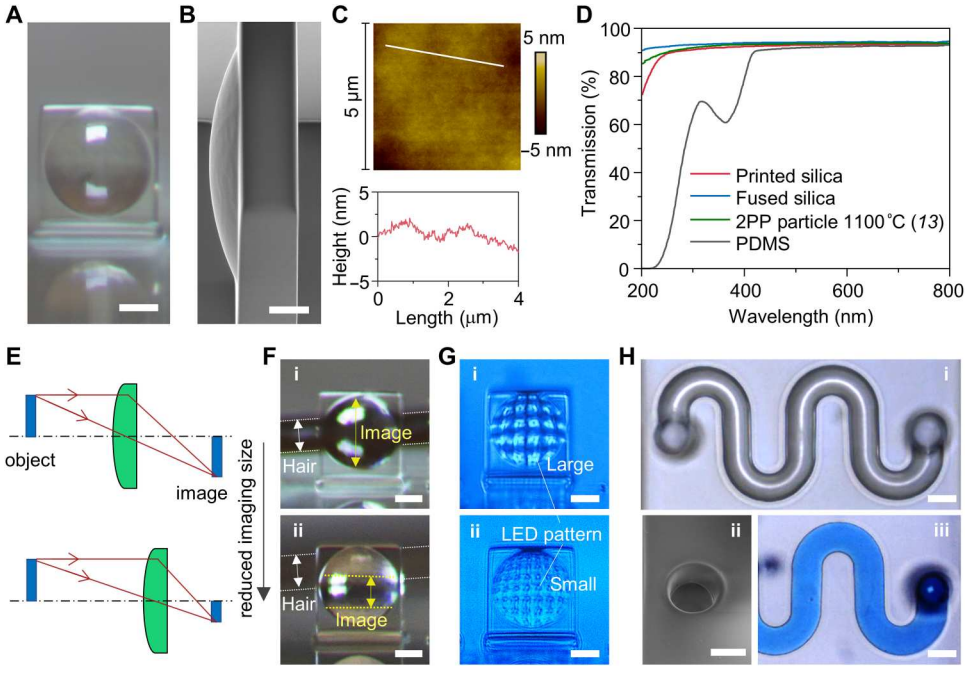

Fig. 4. Applications of the 3D printed silica glass. (**A**) Optical microscope image of the printed silica glass microlens. Scale bar, 50 µm. (**B**) SEM image of the printed silica glass microlens. Scale bar, 20 µm. (**C**) AFM measurement on the printed silica glass, showing very low surface roughness. (**D**) Ultraviolet-visible (UV-Vis) transmission of the printed silica glass compared to commercial fused silica and 2PP-printed silica from particle-containing photoresin (*13*). (**E**) Schematic illustrations of the microlens imaging demonstrations. (**F** and **G**) The microlens imaging demonstrations using a human hair and a patterned LED light. Scale bars, 50 µm. (**H**) The printed silica glass component with a hollow microfluidic channel. Filling with dyed liquid results in no visible change of the microchannel. Scale bars, 30 µm.

(UV-Vis) spectroscopy. The spectrum shows that the printed silica is highly transparent in the range of 200- to 800-nm wavelengths, which is comparable to commercial fused silica glass and 2PP-printed silica glass from particle-containing photoresin (Fig. 4D) (*13*). The discrepancy in the short wavelength range (<250 nm) is attributed to the molecular level vacancies in the printed silica. The measured refractive index (n) is 1.441 ± 0.007 (fig. S20), which is slightly lower than commercial fused silica glass with n = 1.458 (*42*). Our approach also allows for color modifications of the printed silica glass by incorporating inorganic pigments in the PDMS photoresin. For example, doping with chromium(III) chloride ($CrCl_3$) and iron(III) nitrate [$Fe(NO_3)_3$] results in purple-colored and brown-colored glass, respectively (fig. S21). Furthermore, we demonstrate that the printed silica glass lens functions well as an imaging component following the basic principles: the magnification of the image changes with the distance between the target object and the lens (Fig. 4E). We show that the image of a ~60-µm-thick human hair (denoted by the white dotted line) is about twice its actual size when it is placed close to the printed lens (Fig. 4Fi); as the distance between the hair and the lens increases, the image on the lens (denoted by the yellow dotted line) becomes smaller and out of focus (Fig. 4Fii). Similarly, when a patterned light-emitting diode (LED) is used as the target object (see fig. S22 for the experimental setup), a 5 × 5 LED pattern image is observed on the lens, and each LED image is relatively larger when the LED is placed closer to the lens (Fig. 4Gi); as the distance increases, the image pattern becomes denser to a 7 × 7 LED pattern, and each LED image becomes smaller (Fig. 4Gii). These results demonstrate the potential of our printed silica glass as a micro-optics component. Further optimization of the printing algorithms and dedicated lens design are required to achieve the state-of-the-art functionality and imaging quality in the future (*40*).

Silica glass microfluidics offer numerous advantages over their polymeric counterparts, including high resistance to high temperature and pressure, robustness to harsh solvent, optical transparency, and tailorable surface chemistry (*43*). Here, we show that using our technique, 3D glass microfluidic channel with low surface roughness, can be generated (Fig. 4Hi). The diameter of the circular microchannel (Fig. 4Hii) is around 30 µm. Figure 4Hiii displays a dyed methanol liquid filling the microchannel, not resulting in any swelling or leaking of the printed microchannel (see fig. S23 for comparison of swelling behavior between silica glass and PDMS microchannels). Moreover, with a minimum wall thickness of 15 µm, the microfluidic part shows high optical transparency. These properties indicate that the printed glass microfluidics can provide versatile tools for the advance of microfluidic reactors in flow chemistry (*44*).

DISCUSSION

Conventional AM approaches to produce silica structures from nanoparticle-containing polymeric resin use pyrolysis to remove the polymer composition and high-temperature sintering to densify the remaining nanoparticle into silica glass. Here, we present the first photochemistry approach for fabricating 3D silica glass microstructures using DUV-ozone treatment. This approach offers several advantages over conventional AM methods. The conversion to transparent silica glass is performed at moderate

temperatures of 220°C, much lower than conventional sintering temperature. The conversion process is fast and takes less than 5 hours to complete for microscale structures. Distinct from conventional approaches using an intentionally decelerated heat treatment protocol, our approach does not require any additional shrinkage-controlling steps to maintain the microstructure intact during conversion. This fast and low temperature process for printing silica microstructures makes our approach more energy efficient. Furthermore, our photoresin is based on widely used polymer (e.g., PDMS) and can be expanded to other polymers with Si—O, Si—N, and Si—C backbones (*45*, *46*). By tailoring the composition of the polymer backbone with modern synthetic chemistry, glass materials other than SiO_2 can also be potentially made using our approach, for instance, borosilicate glass from boron-containing siloxanes. The resin does not contain any silica nanoparticles, avoiding the potential dispersion-, viscosity-, and optical-related issues associated with conventional methods (*13*). Because the polymer resin is directly converted into silica, our technique is more resource-saving and eco-friendly than conventional methods in which the polymeric phase is burned out during pyrolysis. One step further, our technique can be potentially integrated into state-of-the-art micro/nanomanufacturing technologies. For instance, DUV photolithography techniques are widely used in micro/nanoelectronics manufacturing (*47*). Our mild approach can be adapted into those processes, providing a promising method for in situ fabricating optical microdevices or insulating components.

While our approach offers notable functional advantages, there remain several points that require further improvement for its future development and wider applications. First, the printed silica glass is limited to microstructures with feature dimensions below tens of micrometers, i.e., structures with feature sizes above hundreds of micrometers may require extended conversion time with the current experimental setup. The conversion process relies on the diffusion of excited singlet atomic oxygen $O(^1D)$ into the PDMS network and the decomposed organic species out of the network. Because $O(^1D)$ is quite reactive and short-lived, it has to be generated in situ and diffuse into the network. Hence, the required conversion time is scaled with increasing diffusion path or microstructure feature size (see fig. S24 for detailed relationship). One potential approach to surmount this challenge is to develop specialized DUV light sources. The DUV source used in current study contains large amount of ineffective visible light and exhibits exponential decay as the distance increases. It is anticipated that advanced DUV source featuring a more efficient light spectrum, focused light profile, enhanced light intensity, and optimized light bulb configuration (e.g., 360° circular shape) could significantly enhance the conversion rate and depth and push the printing limit from microscale to bulk scale. Another potential approach to fabricate bulk-scale silica glass structures is through appropriate structure design, for example, hierarchical cellular structures with feature dimensions of tens of micrometers. Alternatively, it is possible to print large-scale structures by formulating versatile PDMS photoresin. In addition, the mechanical and physical properties of the printed silica glass are insufficient for load-carrying applications. The lower modulus of the printed silica compared to fused silica is due to the residual carbon and molecular level vacancies inside. The use of specialized DUV sources with higher intensity and more efficient spectrum can improve the conversion quality as well as the mechanical properties. Additional heat treatment can further densify the silica and increase its modulus (fig. S16). Moreover, while the experimental investigation of the 3D printing process is the primary focus of this study, computational and informatics methods (*48*) are highly desirable to elucidate the underlying photochemistry mechanisms and broaden the material and process choices. For example, upon identifying the key intermediate ozone and reactant singlet atomic oxygen $O(^1D)$ via DFT calculations, the conversion process can be facilitated by purging ozone directly into the glass chamber (fig. S25).

To summarize, we have developed a 3D printing approach to fabricate transparent silica glass microstructures by integrating the 2PP printing technique and DUV-ozone treatment process at mild conditions. Our findings could inspire the exploration of new preceramic chemistries and open up opportunities for future advancement of AM techniques in the realm of polymer-derived ceramics.

MATERIALS AND METHODS

2PP 3D-printing process

PDMS microstructures were fabricated by a 2PP system (Photonic Professional GT2, Nanoscribe GmbH & Co. KG, Eggenstein-Leopoldshafen, Germany) from a commercial PDMS photoresin (IP-PDMS, Nanoscribe GmbH & Co. KG, Eggenstein-Leopoldshafen, Germany) on ITO-coated glass substrate. Before printing, the substrate was cleaned by plasma for 10 min and salinized with 3-(trimethoxysilyl)propyl methacrylate. During printing, the slicing distance, hatching distance, laser power, and writing speed were set to 0.1 to 0.2 μm, 0.2 μm, 20 mW, and 5 to 10 cm/s, respectively. After printing, the PDMS parts were immersed in SU-8 developer for 8 min, followed by two consecutive 1-min rinses in isopropanol alcohol (IPA). Then, the samples were dried slowly under ambient conditions without blowing any air or applying any additional heat treatment. Critical point drying is used to prevent structure collapse caused by capillary effect during IPA evaporation for complex microstructures (for example, the octet microstructures).

DUV-ozone treatment process

Dried PDMS microstructures were converted into silica glass parts using DUV-ozone treatment. A xenon lamp (LH-810, XENON Corp., Wilmington, MA, USA) was used as the DUV source. The light intensity was set to its maximum level (2.5 W/cm^2). The PDMS parts were placed in a glass chamber under DUV irradiation. Excessive amount of oxygen was kept on purging into the chamber. When the desired treatment time was reached, the system cooled down to room temperature and silica glass microstructures were obtained.

Microstructural and compositional characterizations

SEM (SU-8230, Hitachi High-Tech Corp., Tokyo, Japan) equipped with an Oxford EDS detector was used to observe the microstructures and measure their chemical compositions. Digital microscope (VHX-7000, Keyence Corp., Itasca, IL, USA) was used to capture the optical images. FTIR (Nicolet iS5, Thermo Fisher Scientific Inc., Waltham, MA, USA) analysis was conducted to inspect the functional groups upon conversion. Quantitative elemental analysis was performed using an XPS (K-Alpha, Thermo Fisher Scientific Inc., Waltham, MA, USA). The surface roughness was measured

using an AFM (Dimension Icon, Bruker Corp., Billerica, MA, USA). The transmission was characterized using a UV-Vis spectrophotometer (Evolution 220, Thermo Fisher Scientific Inc., Waltham, MA, USA). The thickness of the printed silica and the commercial fused silica (UV-Grade Quartz Plates, Alpha Nanotech Inc., Vancouver, BC, Canada) are 40 μm and 1 mm, respectively. The reflectance was measured by a UV-Vis-NIR spectrometer (AvaSpec-ULS2048CL-EVO, Avantes B.V., Apeldoorn, Netherlands). TGA measurement (Q600, TA Instruments, New Castle, DE, USA) was conducted to determine the thermal stability. The amorphous silica was identified using an XRD (X′Pert Pro Alpha-1, Malvern Panalytical Ltd., Malvern, UK).

Mechanical and physical characterizations

PF-QNM technique in AFM was used to measure the modulus of the converted silica. A standard probe (RTESPA-525-30, Bruker Corp., Billerica, MA, USA) with high spring constant was used after proper tuning and calibration with a standard highly oriented pyrolytic graphite specimen. Young′s modulus was extracted from the force response during the tip retraction from the indentation. The density of the obtained silica glass was calculated by measuring the mass change of a thin-film sample using a high-precision balance and the volumetric change from the SEM photos of microstructures.

DFT calculations

First principles thermodynamics calculations were performed using DFT as implemented in Vienna Ab Initio Simulation Package (*49*, *50*). A plane-wave energy cutoff of 400 eV was used to describe the electronic wavefunctions. van der Waals (vdW) dispersion interaction correction, handled with the nonlocal density functional vdW-D2 (*51*), and the refitted Perdew-Wang 86 (*52*) exchange-correlation functional were used for structure optimization and equilibrium energy evaluation of polymer and organic molecules until atomistic forces became less than 0.01 eV/Å.

Supplementary Materials

This PDF file includes:

Figs. S1 to S25
Table S1

REFERENCES AND NOTES

1. F. Quintero, J. Penide, A. Riveiro, J. del Val, R. Comesaña, F. Lusquiños, J. Pou, Continuous fiberizing by laser melting (Cofiblas): Production of highly flexible glass nanofibers with effectively unlimited length. *Sci. Adv.* **6**, eaax7210 (2020).
2. P. D. García, R. Sapienza, C. López, Photonic glasses: A step beyond white paint. *Adv. Mater.* **22**, 12–19 (2010).
3. P. N. Nge, C. I. Rogers, A. T. Woolley, Advances in microfluidic materials, functions, integration, and applications. *Chem. Rev.* **113**, 2550–2583 (2013).
4. M. N. Rahaman, D. E. Day, B. Sonny Bal, Q. Fu, S. B. Jung, L. F. Bonewald, A. P. Tomsia, Bioactive glass in tissue engineering. *Acta Biomater.* **7**, 2355–2373 (2011).
5. J. E. Shelby, *Introduction to Glass Science and Technology* (Royal Society of Chemistry, ed. 2, 2005).
6. F. Kotz, K. Arnold, W. Bauer, D. Schild, N. Keller, K. Sachsenheimer, T. M. Nargang, C. Richter, D. Helmer, B. E. Rapp, Three-dimensional printing of transparent fused silica glass. *Nature* **544**, 337–339 (2017).
7. M. Mader, O. Schlatter, B. Heck, A. Warmbold, A. Dorn, H. Zappe, P. Risch, D. Helmer, F. Kotz, B. E. Rapp, High-throughput injection molding of transparent fused silica glass. *Science* **372**, 182–186 (2021).
8. F. Kotz, K. Plewa, W. Bauer, N. Schneider, N. Keller, T. Nargang, D. Helmer, K. Sachsenheimer, M. Schäfer, M. Worgull, C. Greiner, C. Richter, B. E. Rapp, Liquid glass: A facile soft replication method for structuring glass. *Adv. Mater.* **28**, 4646–4650 (2016).
9. Y. Hu, S. Rao, S. Wu, P. Wei, W. Qiu, D. Wu, B. Xu, J. Ni, L. Yang, J. Li, J. Chu, K. Sugioka, All-glass 3D optofluidic microchip with built-in tunable microlens fabricated by femtosecond laser-assisted etching. *Adv. Opt. Mater.* **6**, 1701299 (2018).
10. J. Sun, Y. Chen, M. K. Priydarshi, Z. Chen, A. Bachmatiuk, Z. Zou, Z. Chen, X. Song, Y. Gao, M. H. Rümmeli, Y. Zhang, Z. Liu, Direct chemical vapor deposition-derived graphene glasses targeting wide ranged applications. *Nano Lett.* **15**, 5846–5854 (2015).
11. Y. Xu, Y. Li, N. Zheng, Q. Zhao, T. Xie, Transparent origami glass. *Nat. Commun.* **12**, 4261 (2021).
12. D. G. Moore, L. Barbera, K. Masania, A. R. Studart, Three-dimensional printing of multicomponent glasses using phase-separating resins. *Nat. Mater.* **19**, 212–217 (2020).
13. X. Wen, B. Zhang, W. Wang, F. Ye, S. Yue, H. Guo, G. Gao, Y. Zhao, Q. Fang, C. Nguyen, X. Zhang, J. Bao, J. T. Robinson, P. M. Ajayan, J. Lou, 3D-printed silica with nanoscale resolution. *Nat. Mater.* **20**, 1506–1511 (2021).
14. F. Kotz, A. S. Quick, P. Risch, T. Martin, T. Hoose, M. Thiel, D. Helmer, B. E. Rapp, Two-photon polymerization of nanocomposites for the fabrication of transparent fused silica glass microstructures. *Adv. Mater.* **33**, e2006341 (2021).
15. J. T. Toombs, M. Luitz, C. C. Cook, S. Jenne, C. C. Li, B. E. Rapp, F. Kotz-Helmer, H. K. Taylor, Volumetric additive manufacturing of silica glass with microscale computed axial lithography. *Science* **376**, 308–312 (2022).
16. I. Cooperstein, E. Shukrun, O. Press, A. Kamyshny, S. Magdassi, Additive manufacturing of transparent silica glass from solutions. *ACS Appl. Mater. Interfaces* **10**, 18879–18885 (2018).
17. R. Dylla-Spears, T. D. Yee, K. Sasan, D. T. Nguyen, N. A. Dudukovic, J. M. Ortega, M. A. Johnson, O. D. Herrera, F. J. Ryerson, L. L. Wong, 3D printed gradient index glass optics. *Sci. Adv.* **6**, eabc7429 (2020).
18. J. Bauer, C. Crook, T. Baldacchini, A sinterless, low-temperature route to 3D print nanoscale optical-grade glass. *Science* **380**, 960–966 (2023).
19. E. Yarali, C. Koutsiaki, H. Faber, K. Tetzner, E. Yengel, P. Patsalas, N. Kalfagiannis, D. C. Koutsogeorgis, T. D. Anthopoulos, Recent progress in photonic processing of metal-oxide transistors. *Adv. Funct. Mater.* **30**, 1906022 (2020).
20. I. Bretos, R. Jiménez, J. Ricote, M. L. Calzada, Low-temperature crystallization of solution-derived metal oxide thin films assisted by chemical processes. *Chem. Soc. Rev.* **47**, 291–308 (2018).
21. V. M. Graubner, R. Jordan, O. Nuyken, B. Schnyder, T. Lippert, R. Kötz, A. Wokaun, Photochemical modification of cross-linked poly(dimethylsiloxane) by irradiation at 172 nm. *Macromolecules* **37**, 5936–5943 (2004).
22. M. Ouyang, C. Yuan, R. J. Muisener, A. Boulares, J. T. Koberstein, Conversion of some siloxane polymers to silicon oxide by UV/ozone photochemical processes. *Chem. Mater.* **12**, 1591–1596 (2000).
23. C. L. Mirley, J. T. Koberstein, A room temperature method for the preparation of ultrathin SiOx films from langmuir-blodgett layers. *Langmuir* **11**, 1049–1052 (1995).
24. Y. Berdichevsky, J. Khandurina, A. Guttman, Y. H. Lo, UV/ozone modification of poly(dimethylsiloxane) microfluidic channels. *Sens. Actuators B* **97**, 402–408 (2004).
25. Z. Faraji Rad, P. D. Prewett, G. J. Davies, High-resolution two-photon polymerization: The most versatile technique for the fabrication of microneedle arrays. *Microsystems Nanoeng.* **7**, 71 (2021).
26. D. Maji, S. K. Lahiri, S. Das, Study of hydrophilicity and stability of chemically modified PDMS surface using piranha and KOH solution. *Surf. Interface Anal.* **44**, 62–69 (2012).
27. Y. J. Fu, H. Z. Qui, K. S. Liao, S. J. Lue, C. C. Hu, K. R. Lee, J. Y. Lai, Effect of UV-Ozone treatment on poly(dimethylsiloxane) membranes: Surface characterization and gas separation performance. *Langmuir* **26**, 4392–4399 (2010).
28. A. L. Smith, Infrared spectra-structure correlations for organosilicon compounds. *Spectrochim. Acta.* **16**, 87–105 (1960).
29. V. Z. H. Chan, E. L. Thomas, J. Frommer, D. Sampson, R. Campbell, D. Miller, C. Hawker, V. Lee, R. D. Miller, Curious morphology of silicon-containing polymer films on exposure to oxygen plasma. *Chem. Mater.* **10**, 3895–3901 (1998).
30. B. Ulgut, S. Suzer, XPS studies of SiO2/Si system under external bias. *J. Phys. Chem. B* **107**, 2939–2943 (2003).
31. E. Zanchetta, M. Cattaldo, G. Franchin, M. Schwentenwein, J. Homa, G. Brusatin, P. Colombo, Stereolithography of SiOC ceramic microcomponents. *Adv. Mater.* **28**, 370–376 (2016).
32. P. S. Waggoner, C. P. Tan, H. G. Craighead, Atomic layer deposited silicon dioxide films on nanomechanical silicon nitride resonators. *J. Appl. Phys.* **107**, 114505 (2010).
33. S. B. Jin, J. S. Lee, Y. S. Choi, I. S. Choi, J. G. Han, High-rate deposition and mechanical properties of SiO_x film at low temperature by plasma enhanced chemical vapor deposition with the dual frequencies ultra high frequency and high frequency. *Thin Solid Films* **519**, 6334–6338 (2011).

34. R. C. C. Rangel, N. C. Cruz, A. Milella, F. Fracassi, E. C. Rangel, Barrier and mechanical properties of carbon steel coated with $SiO_x/SiO_xC_yH_z$ gradual films prepared by PECVD. *Surf. Coatings Technol.* **378**, 124996 (2019).
35. S. van Kesteren, X. Shen, M. Aldeghi, L. Isa, Printing on particles: Combining two-photon nanolithography and capillary assembly to fabricate multimaterial microstructures. *Adv. Mater.* **35**, 2207101 (2023).
36. Z. Liu, M. Li, X. Dong, Z. Ren, W. Hu, M. Sitti, Creating three-dimensional magnetic functional microdevices via molding-integrated direct laser writing. *Nat. Commun.* **13**, 2016 (2022).
37. J. Bauer, A. Schroer, R. Schwaiger, O. Kraft, Approaching theoretical strength in glassy carbon nanolattices. *Nat. Mater.* **15**, 438–443 (2016).
38. D. W. Yee, M. L. Lifson, B. W. Edwards, J. R. Greer, Additive manufacturing of 3D-architected multifunctional metal oxides. *Adv. Mater.* **31**, 1901345 (2019).
39. Z. Y. Hu, Y. L. Zhang, C. Pan, J. Y. Dou, Z. Z. Li, Z. N. Tian, J. W. Mao, Q. D. Chen, H. B. Sun, Miniature optoelectronic compound eye camera. *Nat. Commun.* **13**, 5634 (2022).
40. S. Thiele, K. Arzenbacher, T. Gissibl, H. Giessen, A. M. Herkommer, 3D-printed eagle eye: Compound microlens system for foveated imaging. *Sci. Adv.* **3**, e1602655 (2017).
41. S. Sivankutty, A. Bertoncini, V. Tsvirkun, N. Gajendra Kumar, G. Brévalle, G. Bouwmans, E. R. Andresen, C. Liberale, H. Rigneault, Miniature 120-beam coherent combiner with 3D-printed optics for multicore fiber-based endoscopy. *Opt. Lett.* **46**, 4968–4971 (2021).
42. I. H. Malitson, Interspecimen comparison of the refractive index of fused silica. *J. Opt. Soc. Am.* **55**, 1205–1209 (1965).
43. K. S. Elvira, X. C. I. Solvas, R. C. R. Wootton, A. J. Demello, The past, present and potential for microfluidic reactor technology in chemical synthesis. *Nat. Chem.* **5**, 905–915 (2013).
44. R. Porta, M. Benaglia, A. Puglisi, Flow chemistry: Recent developments in the synthesis of pharmaceutical products. *Org. Process Res. Dev.* **20**, 2–25 (2016).
45. J. Kim, J. H. Jang, J. H. Kim, K. Park, J. S. Jang, J. Park, N. Park, Inorganic encapsulation method using solution-processible polysilazane for flexible solar cells. *ACS Appl. Energy Mater.* **3**, 9257–9263 (2020).
46. M. S. Chen, C. S. Dulcey, L. A. Chrisey, W. J. Dressick, Deep-UV photochemistry and patterning of (aminoethylaminomethyl) phenethylsiloxane self-assembled monolayers. *Adv. Funct. Mater.* **16**, 774–783 (2006).
47. M. Totzeck, W. Ulrich, A. Göhnermeier, W. Kaiser, Pushing deep ultraviolet lithography to its limits. *Nat. Photonics.* **1**, 629–631 (2007).
48. R. Ramprasad, R. Batra, G. Pilania, A. Mannodi-Kanakkithodi, C. Kim, Machine learning in materials informatics: Recent applications and prospects. *npj Comput. Mater.* **3**, 54 (2017).
49. G. Kresse, J. Furthmüller, Efficiency of ab-initio total energy calculations for metals and semiconductors using a plane-wave basis set. *Comput. Mater. Sci.* **6**, 15–50 (1996).
50. G. Kresse, D. Joubert, From ultrasoft pseudopotentials to the projector augmented-wave method. *Phys. Rev. B.* **59**, 1758–1775 (1999).
51. S. Grimme, Semiempirical GGA-type density functional constructed with a long-range dispersion correction. *J. Comput. Chem.* **27**, 1787–1799 (2006).
52. J. P. Perdew, W. Yue, Accurate and simple density functional for the electronic exchange energy: Generalized gradient approximation. *Phys. Rev. B.* **33**, 8800–8802 (1986).

Acknowledgments

Funding: The support of an ONR grant (N00014-21-1-2258) is acknowledged. This work was performed in part at the Georgia Tech Institute for Electronics and Nanotechnology, a member of the National Nanotechnology Coordinated Infrastructure, which is supported by the National Science Foundation (ECCS-1542174). **Author contributions:** Conceptualization: L. Yue and H.J.Q. Methodology: M.L. and L. Yue. Investigation: M.L., L. Yue, L. Yu, and S.M.M. Software: A.C.R. and H.S. Supervision: H.J.Q. and R.R. Writing—original draft: M.L., L. Yue, and H.J.Q. Writing—review and editing: R.R. **Competing interests:** The authors declare that they have no competing interests. **Data and materials availability:** All data needed to evaluate the conclusions in the paper are present in the paper and/or the Supplementary Materials. Detailed data of DFT calculations are available at https://khazana.gatech.edu/.

Submitted 17 April 2023
Accepted 5 September 2023
Published 4 October 2023
10.1126/sciadv.adi2958